Modeling Pure Methane Hydrate Dissociation Using a Numerical Simulator from a Novel Combination of X-ray Computed Tomography and Macroscopic Data

Arvind Gupta [(1)*, †], *George J. Moridis* [(2)], *Timothy J. Kneafsey* [(2)], *and E.D. Sloan, Jr.* [(1),]

Center for Hydrate Research, Department of Chemical Engineering, Colorado School of Mines, 1600 Illinois Street, Alderson Hall-425, Golden, CO-80401, USA

Earth Sciences Division, Lawrence Berkeley National Laboratory, 1 Cyclotron Road, M.S. 90-1116, Berkeley, CA 94720, USA

* Presently working with Shell Global Solutions International B.V., Amsterdam, The Netherlands

† Corresponding authors:

E-mail: Arvind.Gupta@Shell.Com, Telephone: 0031 (020)-630-2939, Fax: 0031 (020)-630-2235

Abstract

The numerical simulator TOUGH+HYDRATE (T+H) was used to predict the transient pure methane hydrate (no sediment) dissociation data. X-ray computed tomography (CT) was used to visualize the methane hydrate formation and dissociation processes. A methane hydrate sample was formed from granular ice in a cylindrical vessel, and slow depressurization combined with thermal stimulation was applied to dissociate the hydrate sample. CT images showed that the water produced from the hydrate dissociation accumulated at the bottom of the vessel and increased the hydrate dissociation rate there. CT images were obtained during hydrate dissociation to confirm the radial dissociation of the hydrate sample. This radial dissociation process has implications for dissociation of hydrates in pipelines, suggesting lower dissociation times than for longitudinal dissociation. These observations were also confirmed by the numerical simulator predictions, which were in good agreement with the measured thermal data during hydrate dissociation. System pressure and sample temperature measured at the sample center followed the CH_4 hydrate L_w+H+V equilibrium line during hydrate dissociation. The predicted cumulative methane gas production was within 5% of the measured data. Thus, this study validated our simulation approach and assumptions, which include stationary pure methane hydrate-skeleton, equilibrium hydrate-dissociation and heat- and mass-transfer in predicting hydrate dissociation in the absence of sediments. It should be noted that the application of T+H for the pure methane hydrate system (no sediment) is outside the general applicability limits of T+H. This approach is generally not recommended into the regime explored here (no sediment), but it can be considered only after fully evaluating the conditions and being fully aware of the physics and limitations.

Keywords*:* x-ray tomography*,* methane hydrate, heat transfer, simulation, dissociation, depressurization, thermal stimulation

Introduction

Natural gas clathrate hydrates are a class of inclusion compounds formed from a network of water molecules that encapsulate small gas molecules.[1] In general, hydrates form at high pressures and low temperatures in the presence of water and the hydrate former molecule (e.g., methane, ethane, propane). Gas hydrates are mainly studied in five research areas: flow assurance, energy recovery, climate change, safety, and gas storage/transportation. Given the ever-increasing global energy demand and the potential of gas hydrates as a hydrocarbon gas source, scientists have been quite actively involved in hydrate research over the last few years. Gas-hydrate deposits are estimated to contain enormous amounts of hydrocarbons (mainly methane, on the order of 10^{15} m^3 to 10^{17} m^3 at standard temperature and pressure conditions (STP) [2, 3], and dozens of natural deposits have been encountered. These deposits present a potential future energy resource, with recovery of even a fraction of the estimated hydrocarbons contained within the hydrates providing a substantial alternative energy resource. Early efforts to address gas production from hydrate deposits in geologic media faced many challenges, such as lack of engineering expertise to complete wells in hydrate deposits, concerns about the geomechanical stability of dissociating hydrate-bearing sediments, and potential environmental implications. These problems have to be overcome before large-scale gas production from the natural hydrate resources becomes a reality.[4]

Following an earlier study, a field-scale hydrate dissociation test was conducted in 2002 at the Mallik site (Mackenzie Delta, Northwest Territories, Canada). [5] In addition to providing a proof-of-concept for gas production from a permafrost methane hydrate reservoir, this test provided significant initial insights into some of the aforementioned knowledge gaps. Analysis of the observations from this test provided an early indication of the validity of numerical simulation as a predictive tool for the design of methods and operations for gas production from hydrates.[6,7]

Numerical simulation plays a critically important role in the study of recovery of fossil fuels from geologic reservoirs and is expected to play just as important a role in the analysis of all aspects of gas production from hydrate deposits, including the design and analysis of laboratory and field experiments. Several simulators have been developed that have been used to analyze field experiments, [6,8] to determine important parameters through inverse modeling (history matching) of data from laboratory experiments, [9] and to investigate the gas production potential of several types of hydrate deposits. [10,11,12,13,14,15,16]

In the present study, we used the TOUGH+HYDRATE (hereafter referred to as T+H) numerical simulator to model pure methane hydrate dissociation in a laboratory experiment. [17] We compared the measured and modeled transient thermal response and gas evolution from the hydrate during dissociation. The hydrate dissociation data were obtained from x-ray computed tomography analysis combined with simultaneous pressure, temperature, and gas evolution measurements during dissociation. This application of the T+H code involves an extension of its applicability, because the underlying physics in the model assume the presence of a mineral porous medium and mineral grain-to-grain contact. The absence of a mineral porous medium in this study of pure hydrates is circumvented by subdividing the hydrate into two components: (a) the bulk of the hydrate (subject to dissociation and saturation change), and (b) a hydrate "skeleton" that is not exposed to dissociation. In this case, this skeleton is unchanged during most of the experiment's duration and represents a small fraction of the initial hydrate saturation. This acts as a pseudo-porous medium substrate. As the results of this study indicate, this is a reasonable approximation and provides information in support of the T+H code validation.

Experimental Details

Figure 1 shows a schematic of the experimental apparatus used in this study. The experiment was performed in a 7.6 cm i.d. × 26.7 cm long cylindrical x-ray transparent aluminum vessel. A detailed

description of the vessel has been given elsewhere and will not be repeated here. [18,19] The temperature of the vessel was controlled by circulating a water/glycol coolant solution through the PVC jacket surrounding the vessel. A temperature controller was used to maintain the coolant temperature within ± 0.2 K from the desired level. The pressure at the gas inlet line was measured within ±0.007 MPa using a Rosemount 1151 pressure transducer. Four type-T thermocouples (45 cm long, 0.16 cm diameter, Omega Engineering, Stamford CT) were used to measure the thermal response of the hydrate sample. For modeling purposes, the exact position of each thermocouple with respect to the vessel center was determined from the CT images.

We used a modified Siemens Somatom HiQ medical computed tomography (CT) scanner with a peak x-ray beam energy of 133 keV and a current of 120 mA to collect a time series of images of hydrate samples undergoing changes (mainly dissociation, with a corresponding phase saturation redistribution). The CT images provided a measure of material density within a specific volume of about 250 μm x 250 μm × 5mm (called as "voxel"). The CT scanner was calibrated using a set of materials having known densities such as water, air, and aluminum. During hydrate dissociation, CT images were obtained at two different locations at two-minute intervals.

Methane hydrate was synthesized in the vessel from 250–850 μm size granular ice particles using a method similar to that of Stern and coworkers. [20] The ice was packed in layers using a solid cylindrical rod to pack the ice in place. Methane hydrate was formed by slowly pressurizing the vessel (to avoid the ice melting as a result of gas compression) to 6.2 MPa with 99.9% pure methane gas at 265 K. The vessel pressure decreased with time as the methane gas was consumed, owing to hydrate formation in the vessel. After 4 hours, the bath temperature was raised step-wise to the ice point to enhance the hydrate formation by melting the ice. Based on the observed gas consumption and assuming a hydration number equal to 6.0, about 91±2 % (by mass) of the original ice was converted into hydrate over two days. After two days, the bath temperature was increased to 274 K, and any unconverted ice melted into

liquid water. The final product at 274 K was a porous heterogeneous sample composed of (a) a matrix of solid methane hydrate and (b) a pore network filled with a small amount of liquid water and methane gas.

Figure 2 shows the phase diagram for excess water- CH_4- methane hydrate system. The methane hydrate was performed formed under water-limited (excess gas) system. In other words, our system would have been in stable vapor + methane hydrate (if sufficient time was allowed to convert all the water into hydrate) region before the hydrate dissociation process was initiated, but this region is not shown in Figure 2.

Figure 3 shows the axially averaged CT images before and after hydrate formation. Figure 3a shows granular ice (I) and methane gas (G); Figure 3b shows methane hydrate (H), methane gas (G), and water (W). We used the image-processing program ImageJ to convert x-ray attenuation distributions to composite density. [21] Image analysis showed that the composite density was 643 kg/m^3 before hydrate formation. After hydrate formation, the sample composite density increased radially from 420 kg/m^3 to 720 kg/m^3 from the center to the outer perimeter in contact with the vessel wall. The heterogeneity in the sample was attributed to water movement (redistribution) within the sample caused by changes in the capillary pressure during the rapid hydrate formation after ice melted into water. A detailed description of the heterogeneity that occurred during hydrate formation has been offered elsewhere.[22]

Simulation Methodology

The numerical model, TOUGH+HYDRATE

We used the T+H numerical simulator to predict the thermal response of the porous hydrate sample, in addition to the evolution of the methane release during dissociation.[17] The simulator can model the nonisothermal hydration reaction (dissociation) and the flow of water, gas, and heat in a porous medium.

The simulator accounts for heat and up to four mass components (i.e., water, CH_4, hydrate, and water-soluble inhibitors) that can be distributed among four phases: gas, aqueous, ice, and hydrate. The simulator can model any combination of the possible hydrate dissociation mechanisms, i.e., depressurization, thermal stimulation, and chemical inhibition.

In T+H, the hydration reaction (dissociation) can be treated either as equilibrium or as a kinetic process. In the equilibrium option, the hydrate is just one state of the CH_4+H_2O system. The components CH_4+H_2O are distributed among the various phases and states based on the pressure (P), temperature (T), and total enthalpy. In the kinetic model, the hydrate is a chemical compound (in addition to being a phase) that reacts to changes in P and/or T to release CH_4 and H_2O. Bishnoi and coworkers developed an intrinsic kinetic-rate equation for methane hydrate dissociation. [23] They proposed that the decomposition rate is proportional to the specific area of the hydrate surface, A_{HS} (surface area per unit hydrate volume), and a fugacity driving force—the difference between the fugacity of methane at the three-phase equilibrium conditions, f_e, and the fugacity of methane in the gas phase, f_g, accordingly:

$$\frac{-dn_H}{dt} = k_d * A_{HS} * \left(f_e - f_g\right) \qquad \text{Equation 1}$$

The decomposition constant k_d has an Arrhenius-type temperature dependence coefficient k_d^o, with the activation energy ΔE_a as follows:

$$k_d = k_d^o * Exp\left(-\Delta E_a \big/ RT\right) \qquad \text{Equation 2}$$

Recently, Moridis et al. used a history-matching technique to estimate the kinetic parameters of methane hydrate dissociation in porous media. [11] Their work concluded that the estimated activation energy (ΔE_a) and intrinsic dissociation (k_d^o) rate constant was between one and two orders of magnitude larger than the reported literature values from Bishnoi and coworkers. [23, 24] In this study we used the equilibrium model in our hydrate dissociation simulations because early P and T measurements showed that the system dissociated along the L_w+H+V methane hydrate equilibrium line (see Figure 2).

Additionally, recent studies have shown the practical coincidence of solutions based on equilibrium and kinetic dissociation. [25]

Numerical grid

The vessel and sample were oriented horizontally, and the need to account for gravitational effects (i.e., water drainage and gas accumulation at the upper portion of the horizontally lying cylinder) precluded using a radial grid and necessitated using a Cartesian 2D grid. The CT images confirmed that the water originating from hydrate dissociation collected at the bottom of the vessel due to gravity. This water influenced the rate of heat transfer from the bath to the hydrate sample (discussed in Results Section). The assumption of uniformity along the cylinder axis (which alleviated the need for a 3D grid) was reasonable because (a) heat transfer through the metal vessel walls was radial, and (b) CT data showed hydrate saturation distribution to be radially symmetrical (see discussion in Experimental Section). This uniformity allowed the simulation of the actual domain as a single slice with a $\Delta y = 26.7$ cm (i.e., equal to the vessel length), thus significantly reducing the problem and the execution time. The domain was discretized into 20×40 subdivisions in (x,z), resulting in a total of 800 gridblocks, as shown in Figure 4a. This mesh was further modified to replicate the cylindrical geometry of the pressure vessel by removing the cells lying outside the outer radius of the cylindrical vessel (see Figure 4b). Finally, because of symmetry about the z-axis (vertical central line), only half of the system was simulated. The result of this successive reduction was a relatively small grid that kept the execution times (of the computationally demanding simulation of dissociating hydrates) within manageable limits.

Boundary and initial conditions

The boundary at the outer surface of the aluminum vessel was maintained at a constant temperature T_B, i.e., that of the bath surrounding the vessel. The aluminum pressure vessel was simulated as an impermeable (no-flow) boundary that allowed conductive heat exchange with the hydrate sample.

Because of the high thermal conductivity of aluminum, we assumed that the measured bath temperature was equal to the aluminum vessel temperature during the entire dissociation experiment.

The T+H code is designed for the simulation of hydrate behavior in geologic media, and the underlying equations are based on the physics of heat and mass flow and transport through porous media. Thus, the application of Darcy's law (the basic equation describing subsurface fluid flow) is based on the assumption of the presence of a porous sediment having grain-to-grain contact. This is not the case in our study, in which a pure hydrate sample is analyzed. Because the hydrate-related physics and thermodynamics in the T+H code are unaffected by the physics of flow through porous media, the range of applicability for the code is extended to the simulation of the behavior of a porous sample of pure hydrate. No sediment was present in our sample; the porous medium here (i.e., the equivalent of grains in a sediment) is composed of methane hydrate particles (formed from the hydration reaction of the original ice particles and CH_4), and the pore spaces are filled with water and gas. The assumption of code applicability to this type of medium is based on the approximation that there is a hydrate skeleton (at the center of the sample) that, unlike the rest of the hydrate, resists dissociation and remains unchanged during the experiments. This skeleton, acting as a pseudo-porous medium and constituting a small fraction of the system volume, providing a large porosity for the pseudo-porous medium, which in our simulations was taken to be equal to $\phi = 0.999$. The pores of the pseudo-porous medium are filled with nonsediment phases (i.e., hydrate, water, and gas). Two obvious shortcomings of this approach are that (1) the skeleton of the pseudo-medium has to be sufficiently extensive to support the conventional physics of flow through porous media, and (2) it cannot be valid when the sample approaches complete dissociation (open system). The flow in open systems is not governed by Darcy's Law, but a reasonable approximation is obtained by assigning a very large permeability (1, 000 to 10, 000 Darcies) to the open domain. This approximation is standard in simulations of fluids through wellbores, and the results are generally in good agreement with those obtained from open wellbore model. [15]

The permeability of the system changes as a function of the hydrate saturation according to the model of Verma and Pruess.[26] The process for accounting for the changing absolute and relative permeability as the hydrate saturation decreases is fully described by Moridis et al. [17]

To account for the heterogeneity in the radial direction (see Figure 3b), we divided the sample into two separate zones characterized by different hydrate, water, and gas saturations (S_H, S_A and S_G, respectively). The two zones were identified from CT scans, which also provided estimates of the S_H, S_A, and S_G distributions in the two zones (see Figure 3b). The initial S_H, S_A, and S_G in the porous methane hydrate sample are listed in Table 1. These initial saturation estimates were calculated by matching the bulk density estimated using CT images and mass balance.

The water properties in the T+H code are computed from steam tables contained in the code. [17] The properties of the gas phase (which is mostly CH_4, with a small fraction of water vapor) are computed using the Peng-Robinson equation of state (one of the options in T+H). Methane hydrate properties such as heat capacity, thermal conductivity, density, and hydration number have been obtained from the extensive data included in Sloan and Koh. [1]

Results and Comparison with Simulation Predictions

Experimental results

The porous hydrate sample was dissociated by a combination of slow depressurization and thermal stimulation. System pressure and temperatures at four locations within the sample were continuously monitored during the dissociation process. In addition, the flow rate of the gas that evolved from the hydrate dissociation with time was measured.

At t = 0, the system temperature was 279.2 K and the pressure was 4.78 MPa, which is equal to the methane hydrate equilibrium pressure. Thus, the system initially was on the CH_4 hydrate L_w+H+V

equilibrium line. Using the backpressure regulator, we slowly decreased the system pressure from 4.78 MPa to 3.1 MPa over 248 minutes, at a rate described by the following equation (fit to pressure):

$$P = 4.78 * Exp\left(-3 * 10^{-5} * t\right) \qquad \text{Equation 3}$$

where P is the pressure (MPa) and t is the time (seconds). The boundary (or bath) temperature (i.e., T_B) was held constant at 279.2 K throughout the dissociation experiment. Because of the endothermic nature of hydrate dissociation, the hydrate sample temperature decreased from 279.2 K to 275.1 K, but always remained above the water freezing point because system pressure was maintained above the CH_4-hydrate quadruple-point pressure.

Figure 5 shows subcooling as a function of time at three locations. Subcooling is defined as the difference between the CH_4-hydrate equilibrium temperature at system pressure (T_e) and the sample temperature (T) measured at different locations, and described by the following equation:

$$\text{Subcooling} = T_e - T \qquad \text{Equation 4}$$

The T_e is calculated using the Gibbs energy minimization program, CSMGem. [27] When subcooling is zero, the system remained stable on the L_w+H+V equilibrium line and if the subcooling is negative, then hydrate is unstable and dissociates into gas and water. For the first 150 minutes, the subcooling at the three thermocouples locations remained very close to zero and varied maximally within 0.1 K. After 150 minutes, the temperature at the edge (T_{edge}) began to increase (the subcooling became more negative), indicating that hydrate dissociation had completed or the hydrate dissociation front had passed the edge thermocouple (see Inset B in Figure 5).

During dissociation, CT images were alternately taken at two different locations (25 mm apart in the axial direction) every 2 minutes. Figure 6a shows the advancing radial dissociation front moving toward

the vessel center with time. The hydrate near the vessel wall dissociated first because of its proximity to the heat source. Water released from hydrate dissociation was imbibed in the center of the sample and accumulated in the lower part of the vessel. The density at the hydrate sample center increased from 300 kg/m^3 to 900 kg/m^3 between 0 and 137 minutes. This tripling of density can be also attributed to water migrating toward the center of the sample.

Figure 6b shows the change in the density from 0 minute to 260 minutes along the cross section shown in Image 1 of Figure 6a. The plot shows the progression of the dissociation front with time, i.e., with a darker region (denoting a lower density and an evolving gas phase) expanding at the top, and a brighter region (reflecting the higher density caused by water drainage and accumulation) expanding at the bottom of the system.

Figure 7 shows a comparison between the CT images taken at two locations (located at 118 mm and 143 mm from one end of the vessel) to illustrate the changes in the hydrate sample that occurred during the hydrate dissociation process. [28] Density differences between the initial condition (at t = 0) and at different times during dissociation were determined by subtracting calibrated density values. At both locations, CT data showed the same dissociation-related pattern: radial dissociation and gas accumulation at the top, and water accumulation at the bottom of the vessel because of buoyancy and drainage. The relatively large increase in density at the center (at the location y = 143 mm) may have been caused by the initially low-density sample center. Dark and light semicircular arcs in Figure 7 are from a slight shift in the physical system between the first and subsequent images. The similar dissociation characteristics at the two different locations along the y-axis suggested axially homogeneous dissociation during the experiment, and validated our assumption of axial uniformity (see Numerical Grid Section).

In Figure 8, the system pressure and temperature at the center, T_{center} is compared to the CH_4-hydrate three-phase L_w+H+V equilibrium conditions during the hydrate dissociation. The objective of this plot is to show that how the system P, T conditions respond with respect to methane hydrate equilibrium during the slow-depressurization-induced hydrate dissociation. The plot shows that the system was initially on the stable hydrate region (at t = 0 minute in Figure 5). Note that the subcooling up to of 0.2 K was ignored. For the rest of the dissociation process, the P, T conditions at the center followed the L_w+H+V equilibrium line. Whereas, the P, T conditions at the edge thermocouple moved to the right of the equilibrium curve (no hydrate region) after the hydrate dissociation front passed edge thermocouple.

CT images showed that the hydrate dissociation front moved radially inward, towards the center, and the hydrate near the to wall dissociated first. Hydrate at the center of the sample did not dissociate during the time we observed the dissociation process (see Figure 6). The heat available of dissociating the hydrate is supplied by the bath (which was set constant at 279.1 K) and the hydrate sample itself. The part of the hydrate sample that did not dissociate (mainly towards the center) transfers its internal energy to the sample section where the hydrate was dissociating. In other words, the undissociated hydrate sample transferred heat from the center to the hydrate dissociation front as temperature dropped, and followed the L_w+H+V equilibrium conditions. This P-T data obtained during the dissociation process justified our assumption of using the equilibrium model in the simulations compared to kinetic dissociation model.

Comparison between T+H predictions and the measured data

A comparison between the predicted and the measured temperature response at the edge and the center thermocouples is shown in Figure 9. The predicted and the measured temperatures are in good agreement. This concordance indicated that the T+H simulator accurately captured the decrease in the sample temperature caused by the endothermic nature of the hydrate dissociation process during the earlier part of the experiment (when the assumption of a pseudo-porous medium based on a core

minimal hydrate skeleton is more valid, since less of the hydrate is disturbed). The good agreement between predictions and observations provides validation for the assumption of code applicability beyond the code's normal range, to systems in which sediments do not constitute the porous media (i.e., in systems in which the hydrate plays the dual role of a solid phase and a pseudo-porous medium).

Figure 10 shows the comparison between the CT images and the predicted density profile at time intervals, i.e. 0, 75, 150 and 220 minutes during hydrate dissociation. Due to the symmetry along the X-Z direction, only half of the system was simulated and presented in Figure 10. The simulated results are consistent with the CT images (except at the center) which showed that the density decreased at the top section of the sample due to increased gas saturation, and increased at the bottom due to accumulation of water after 150 minutes. However, the simulated density profile at the central region did not match the CT images, which might due to the absence of any reliable capillary and permeability data and models for pure hydrate systems. The images also confirmed the radial dissociation of the hydrate sample as the density close to the vessel boundary changed during dissociation.

Figure 11 shows a comparison between the observed and predicted volumes of the released methane gas. The produced gas included CH_4 originating from both the hydrate dissociation and the initial free gas in the system. Based on the simulation results, the collected methane gas corresponds to about 43% of the initial hydrate mass dissociating during the 220 minutes of the experiment. Initially, the simulator slightly overpredicted the CH_4 production, but the trend reversed after 180 minutes. At the end of the experiment, the deviation between observations and predictions was less than 5%, as calculated from $[(V_{measured}-V_{predicted})/V_{measured} *100]$. The good agreement between the simulation and prediction validates the model and our approach of simulating the porous methane hydrate sample using the T+H code.

Conclusions

X-ray CT imaging was used to visualize the dissociation of a heterogeneous porous methane hydrate sample. Dissociation was induced by slow depressurization combined with thermal stimulation from a constant temperature source. CT images confirmed that the dissociation occurred radially inwards (towards the center of the porous hydrate sample). Water produced from the dissociation of hydrates accumulated at the bottom of the vessel, whereas the top section of the vessel was filled with methane gas. The collected water increased the heat transfer from the bath at the bottom and caused faster hydrate dissociation compared to the top section. Because of the endothermic nature of the hydrate dissociation, the hydrate sample temperature decreased from 279.2 K to 275.1 K, and this temperature decline follows the CH_4-hydrate L_w+H+V equilibrium conditions.

The TOUGH+HYDRATE simulator was used to model the porous methane hydrate dissociation process. The equilibrium dissociation model was used to predict the thermal response and methane gas evolution during dissociation. The predicted thermal response of the sample and methane gas evolution during dissociation was in good agreement with the measured data. Thus, this study validated our simulation approach and assumptions, which include stationary pure methane hydrate-skeleton, equilibrium hydrate-dissociation and heat- and mass-transfer in predicting hydrate dissociation in the absence of sediments. It should be noted that the application of T+H for the pure methane hydrate system (no sediment) is outside the general applicability limits of T+H. This approach is generally not recommended into the regime explored here (no sediment), but it can be considered only after fully evaluating the conditions, but with the expectation that deviation between the model and data will be inevitable once the operating assumptions become invalid.

Acknowledgements

The authors wish to acknowledge the financial support received from the CSM hydrate consortium including BP, Shell, ExxonMobil, Chevron, Halliburton, Statoil, and ConocoPhillips. The laboratory component of this study and the development of the TOUGH+HYDRATE code were supported by the Assistant Secretary for Fossil Energy, Office of Natural Gas and Petroleum Technology, through the National Energy Technology Laboratory, under the U.S. Department of Energy contract with the Lawrence Berkeley National Laboratory, Contract No. DE-AC02-05CH11231. Thanks are due to Liviu Tomutsa for helping with the CT measurements.

References

1) Sloan Jr., E.D. and Koh, C.A., 2008. Clathrate Hydrates of Natural Gases, Third Edition, CRC Press, Boca Raton, FL, 721 pp., and software.

2) Klauda, J.B. and Sandler, S.I., 2005. Global Distribution of Methane Hydrate in Ocean Hydrate. Energy & Fuels, 19: 459-470.

3) Milkov, A.V., 2004. Global Estimates of Hydrate-Bound Gas in Marine Sediments: How much is really out there? Earth Science Reviews, 66, 183-197.

4) Dallimore, S.R. and Collett, T.S., 2005. Scientific Results From The Mallik 2002 Gas Hydrate Production Research Well Program, Meckenzie Delta, Northwest Territories, Canada, Bulletin 585, Geological Survey of Canada.

5) Dallimore, S.R., Uchida, T., and Collett, T.S. (eds.), 1999: Scientific Results from JAPEX/JNOC/GSC Mallik 2L-38 Gas Hydrate Research Well, Mackenzie Delta, Northwest Territories, Canada, Geological Survey of Canada Bulletin 544.

6) Moridis, G.J., T.S. Collett, S.R. Dallimore, T. Inoue and T. Mroz, 2005a. Analysis and Interpretation of the Thermal Test of Gas Hydrate Dissociation in the JAPEX/JNOC/GSC et al. Mallik 5L-38 Gas Hydrate Production Research Well, (LBNL-57296) in Scientific Results from the Mallik 2002 Gas Hydrate Production Research Well Program, Mackenzie Delta,

Northwest Territories, Canada. Geological Survey of Canada, Bulletin 585, S.R. Dallimore and T. Collett, Editors.

7) Kurihara, M., Funatsu, K., Ouchi, H., Masuda, Y., and Narita, H., 2005b, Investigation of Applicability of Methane Hydrate Production Methods to Reservoirs With Diverse Characteristics, Paper 3003, in Proceedings of the 5th International Conference on Gas Hydrates, June 13–16, Trondheim, 714.

8) Kurihara, M., H. Ouchi, T. Inoue, T. Yonezawa, Y. Masuda, S.R. Dallimore, and T.S. Collett, 2005a. Analysis of the JAPEX/JNOC/GSC et al. Mallik 5L-38 Thermal Production Test Through Numerical Simulation, in Scientific Results from the Mallik 2002 Gas Hydrate Production Research Well Program, Mackenzie Delta, Northwest Territories, Canada. Geological Survey of Canada, Bulletin 585, S.R. Dallimore and T. Collett, Editors.

9) Moridis, G.J., Seol, Y., Kneafsey, T., 2005b. Studies of Reaction Kinetics of Methane Hydrate Dissociation in Porous Media, (LBNL-57298) Proc. 5th International Conference on Gas Hydrates, Trondheim, Norway, June 13-16, 2005, Paper 1004, 1: 21-30.

10) Moridis, G.J., 2003. Numerical Studies of Gas Production From Methane Hydrates, (LBNL-49765) SPE Journal, 32(8): 359.

11) Moridis, G.J., T. Collett, S. Dallimore, T. Satoh, S. Hancock and B. Weatherhill, 2004. Numerical Studies Of Gas Production From Several Methane Hydrate Zones At The Mallik Site, Mackenzie Delta, Canada, (LBNL-50257) Journal of Petroleum Science Engineering, 43: 219.

12) Pooladi-Darvish, P., 2004. Gas Production from hydrate reservoirs and its modeling. Journal of Petroleum Technology, Distinguished Author Series, 65-71.

13) Moridis, G.J., Kowalsky, M.B., Pruess, K., 2005c, Depressurization-Induced Gas Production From Class 1 Hydrate Deposits, (LBNL-59780), SPE Journal of Reservoir Evaluation & Engineering, 10(5), 458-481, 2007.

14) Moridis, G.J., Reagan, M.T., 2007a. Gas Production From Oceanic Class 2 Hydrate Accumulations, OTC 18866, 2007 Offshore Technology Conference, Houston, Texas, U.S.A., 30th April–3rd May.

15) Moridis, G.J., Reagan, M.T., 2007b. Strategies for Gas Production From Oceanic Class 3 Hydrate Accumulations, OTC 18865, 2007 Offshore Technology Conference, Houston, Texas, U.S.A., 30th April–3rd May.

16) Moridis, G.J., Sloan, E.D., 2007. Gas Production Potential of Disperse Low-Saturation Hydrate Accumulations in Oceanic Sediments, (LBNL-52568) Journal of Energy Conversion & Management, 48(6): 1834-1849.

17) Moridis, G.J., Kowalsky, M.B., and Pruess, K., 2008c. TOUGH+HYDRATE v1.0 User's Manual: A Code for the Simulation of System Behavior in Hydrate-Bearing Geologic Media, Report LBNL-00149E, Lawrence Berkeley National Laboratory, Berkeley, CA.

18) Kneafsey, T.J. et al., 2005. Methane hydrate formation and dissociation in a partially saturated sand-measurements and observations. Fifth International Conference on Gas Hydrates, 1033: 213-220.

19) Kneafsey, T.J. et al., 2007. Methane Hydrate Formation and Dissociation in a Core-Scale Partially Saturated Sand Sample. Journal of Petroleum Science and Engineering, 56: 108-126.

20) Stern, L.A., Kirby, S.H. and Durham, W.B., 1996. Peculiarities of methane clathrate hydrate formation and solid-state deformation, including possible superheating of water ice. Science, 273: 1843.

21) Abramoff, M.D., Magelhaes, P.J., and Ram, S.J., 2004, Image Processing with ImageJ, Biophotonics International, 11 (7): 36-42.

22) Gupta, A., Kneafsey, T.J., Moridis, G.J., Seol, Y., Kowalsky, M.B., Sloan, E.D. Jr., 2006. Composite Thermal Conductivity in a Large Heterogeneous Porous Methane Hydrate Sample, Journal of Physical Chemistry-B, 110: 16384-16392.

23) Kim, H.C., Bishnoi, P.R., Heidemann, R.A. and Rizvi, S.S.H., 1987. Kinetics of Methane Hydrate Decomposition. Chemical Engineering Science, 42, 7: 1645-1653.

24) Clarke, M.A. and Bishnoi, P.R., 2001. Determination of the activation energy and intrinsic rate constant of methane gas hydrate decomposition. Canadian Journal of Chemical Engineering, 79: 143-147.

25) Kowalsky, M.B., and Moridis, G.J., 2007. Comparison of Kinetic and Equilibrium Reaction Models in Simulating the Behavior of Gas Hydrates in Porous Media, Journal of Energy Conversion and Management, 48(6): 1850-1863.

26) Verma, A. and K. Pruess, 1988. Thermo-hydrologic Conditions and Silica Redistribution Near High-Level Nuclear Wastes Emplaced in Saturated Geological Formations, *J. of Geophys. Res.*, Vol. 93, No. B2, pp. 1159-1173.

27) Ballard, A.L. and Sloan, E.D., Jr., 2002. The next generation of hydrates prediction I. Hydrate standard states and incorporation of spectroscopy. Fluid Phase Equilibria, 194-197: 371-383.

28) Gupta, A., 2007, Methane Hydrate Dissociation Measurements and Modeling: The Role of Heat Transfer and Reaction Kinetic, PhD thesis, Colorado School of Mines, Golden, Colorado, USA.

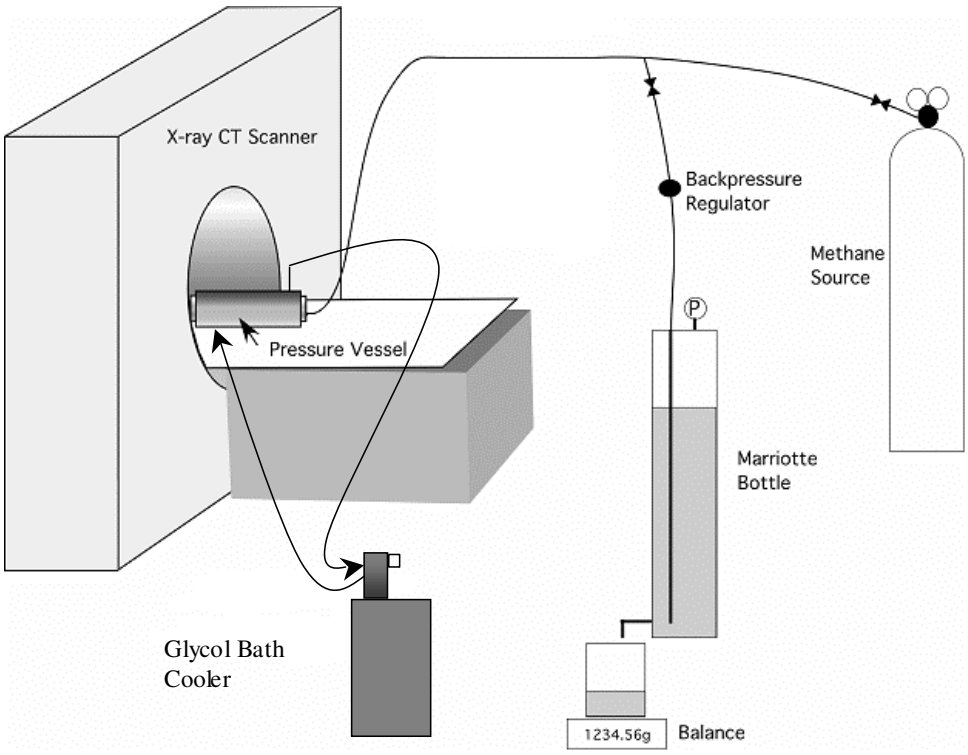

Figure 1. Schematic diagram of the experimental setup used for hydrate dissociation.

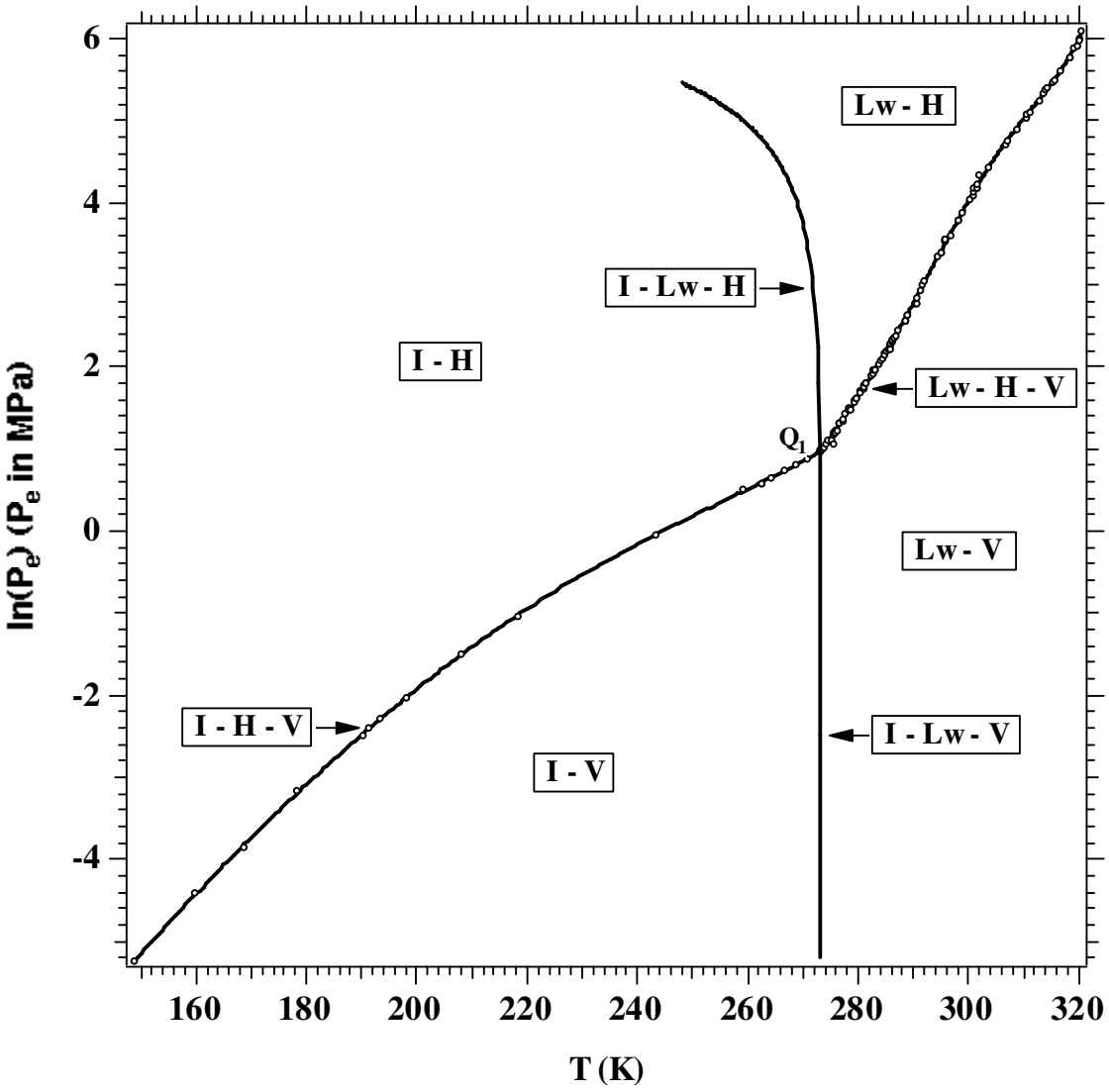

Figure 2. The phase diagram of excess water- CH_4 - hydrate system. The existence of aqueous (L_w), ice (I), gas (V), and hydrate (H) phases, and the combinations thereof, are indicated. Note the natural logarithmic scale on the y-axis.

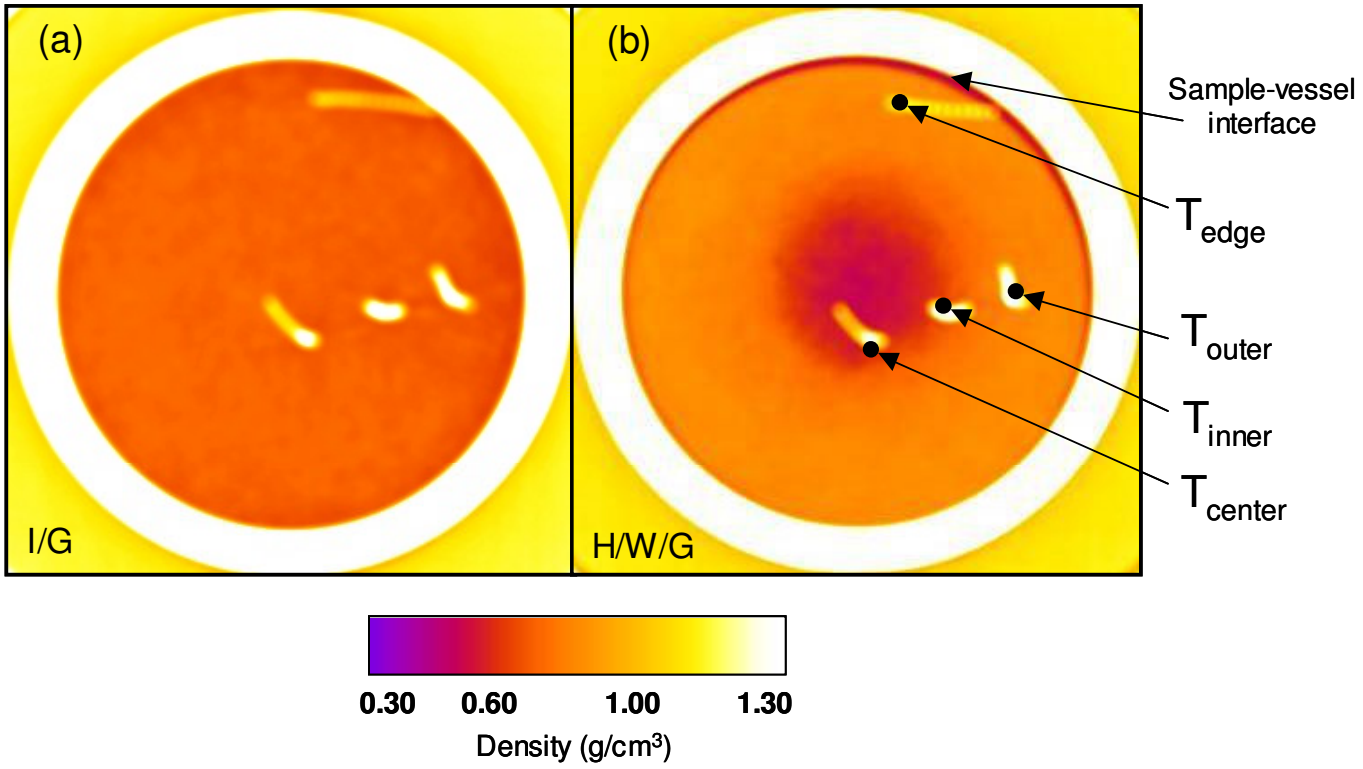

Figure 3. Average X-ray CT images of 51 (out of 54) cross sections, before (left) and after hydrate formation (right). Four white spots show the locations of thermocouple inserted in the sample.

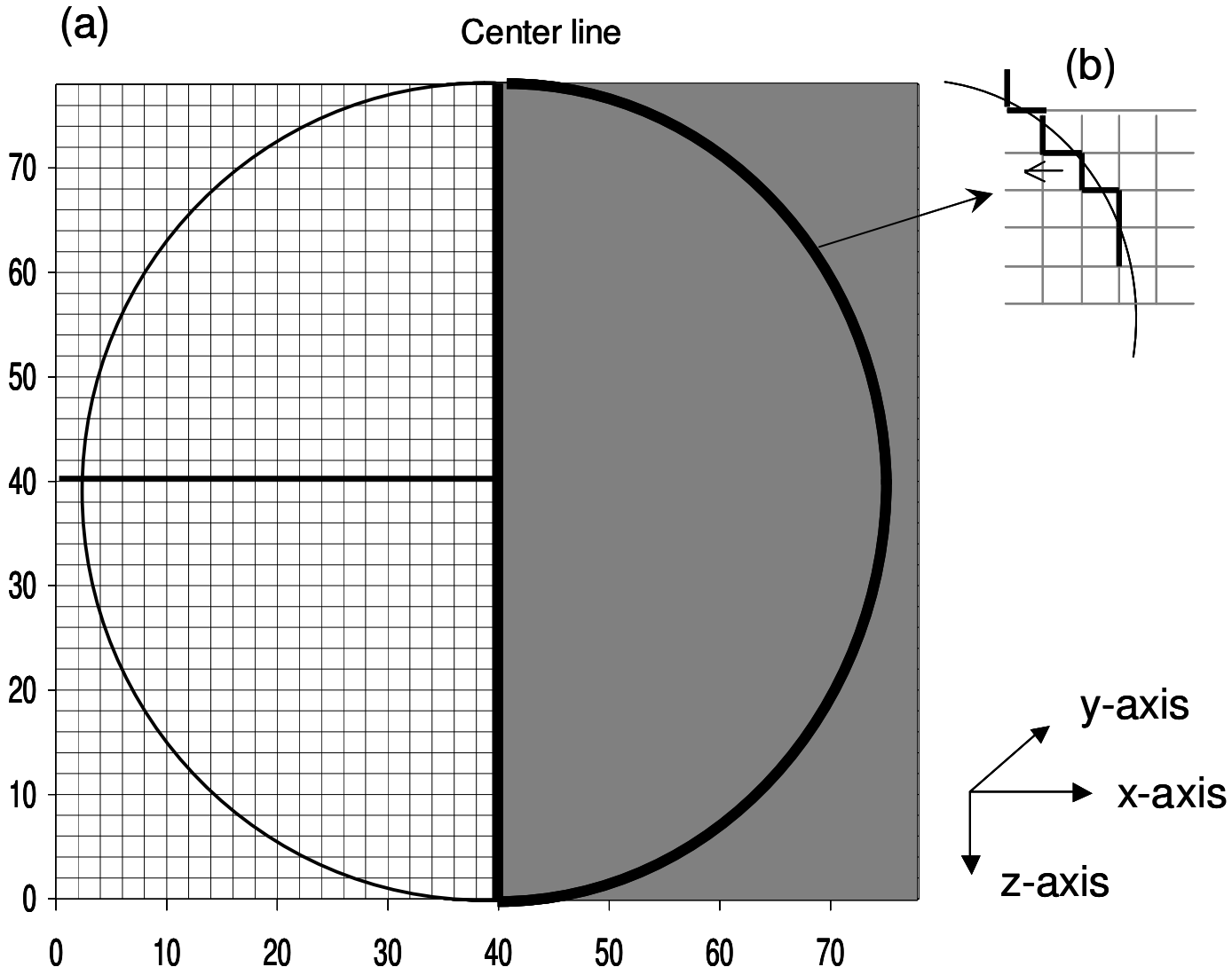

Figure 4. (a) Grid structure for simulating the cylindrical aluminum pressure vessel in x-z direction. Due to symmetry in x- z direction, only the shaded section was simulated. Each gridblock dimension is 2 mm x 26.7 cm x 2 mm in the x, y, and z directions, respectively. (b) This subplot shows the boundary gridblocks adjusted to replicate the cylindrical geometry of the vessel using the Cartesian gridblocks.

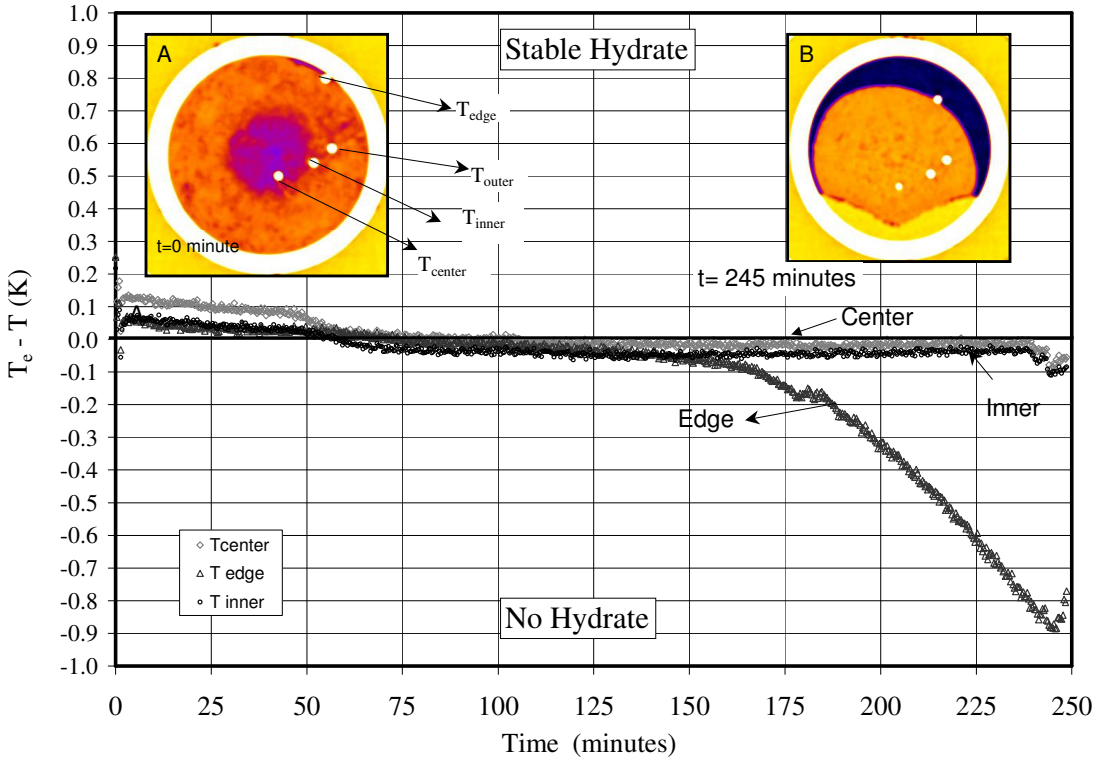

Figure 5. Measured subcooling at the three-thermocouple locations (edge, inner, and center as shown in Inset A) as a function of time. CT images shown in Insets A and B visualize the position of the thermocouple at 0 and 245 minutes during dissociation, respectively. Note that the subcooling up to of 0.2 K was ignored.

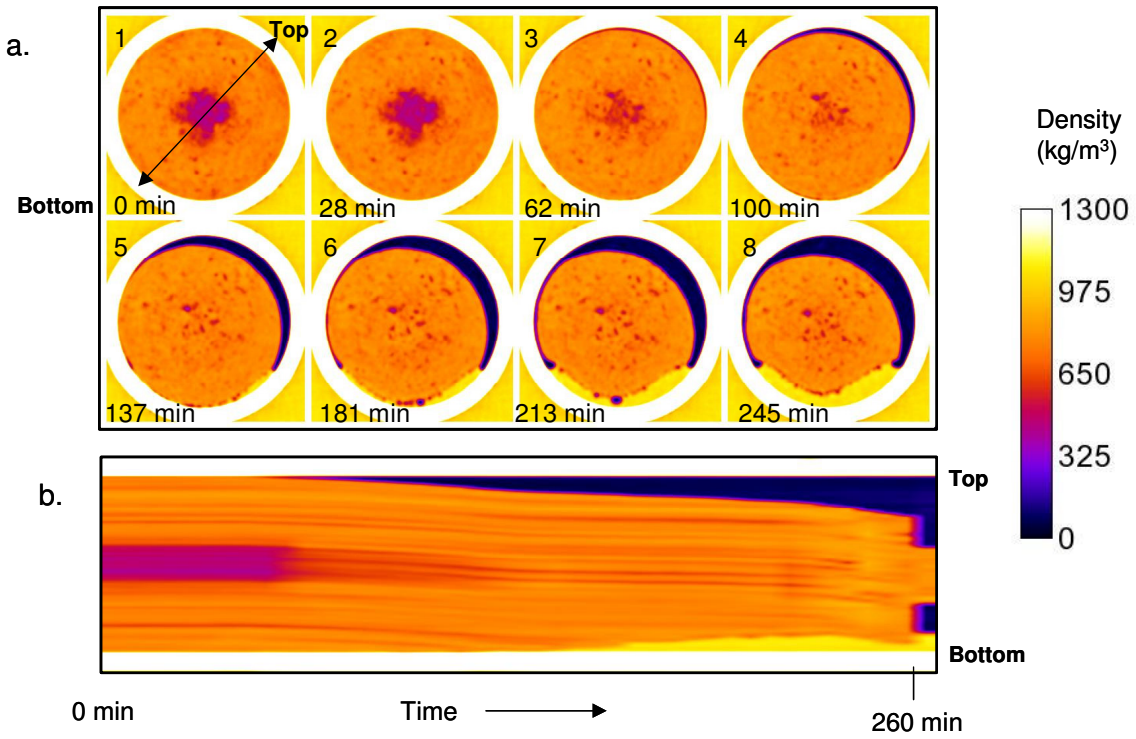

Figure 6. (a) CT images from one location at different times during hydrate dissociation. The white circle is the aluminum pressure vessel. The dark crescent (in Images 4, 5, 6, 7, and 8) close to the vessel wall shows the appearance of the gas phase due to hydrate dissociation. (b) Temporal changes along the cross section shown in Image 1. Plot consists of 40 sequential images and shows density changes with time. Density increases are brighter (e.g. yellow) and decreases are darker (e.g. blue).

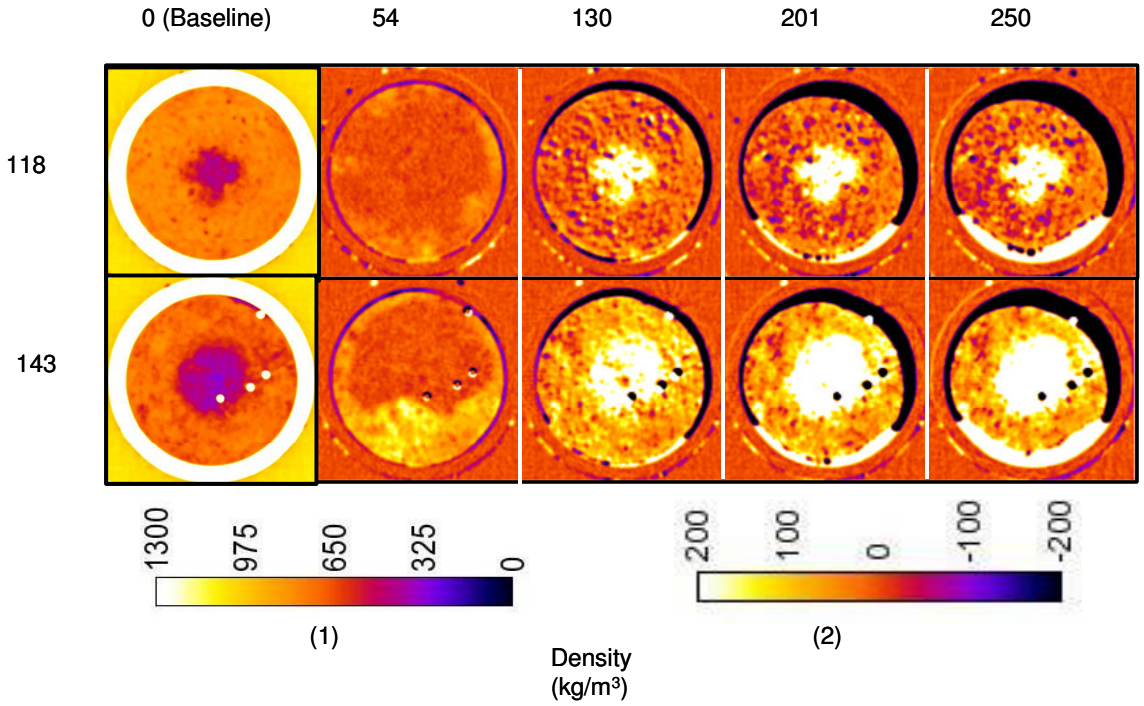

Figure 7. CT images at two locations (118 and 143 mm from one end) at different times during hydrate dissociation. The baseline images show sample density distribution at t=0. CT images at different times (54, 130, 201, and 250 minutes) show density changes during hydrate dissociation. The baseline CT image density distribution corresponds to density bar (1), and the rest of the CT images relative to density bar (2).

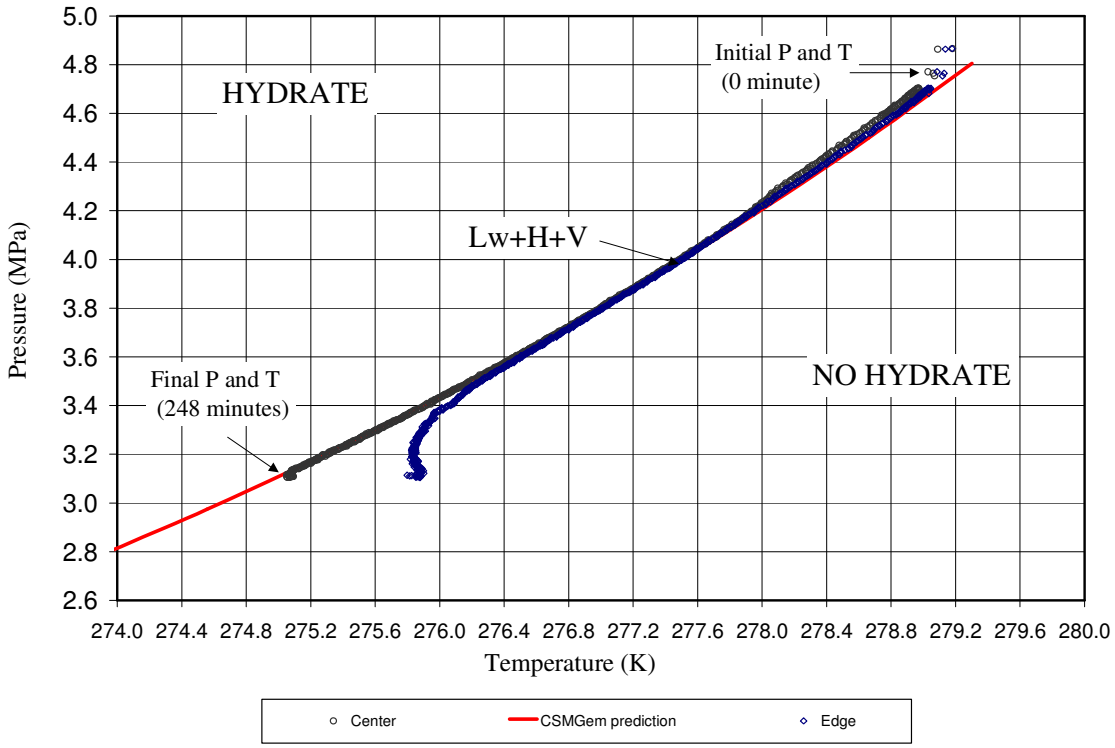

Figure 8. Comparison of methane hydrate three-phase equilibrium curve (L_w+H+V) and the measured pressure and temperatures (using the center and the edge thermocouple).

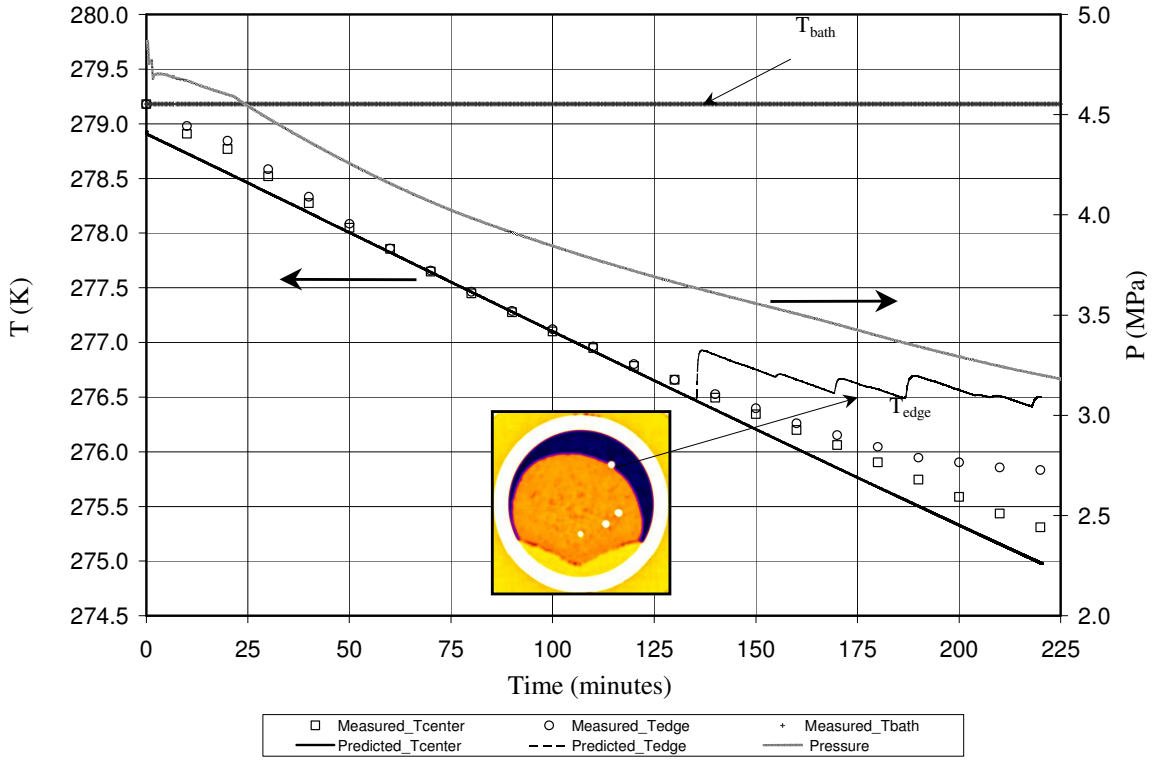

Figure 9. Comparison of predicted and measured temperature curves of the porous hydrate sample with time during depressurization-induced dissociation.

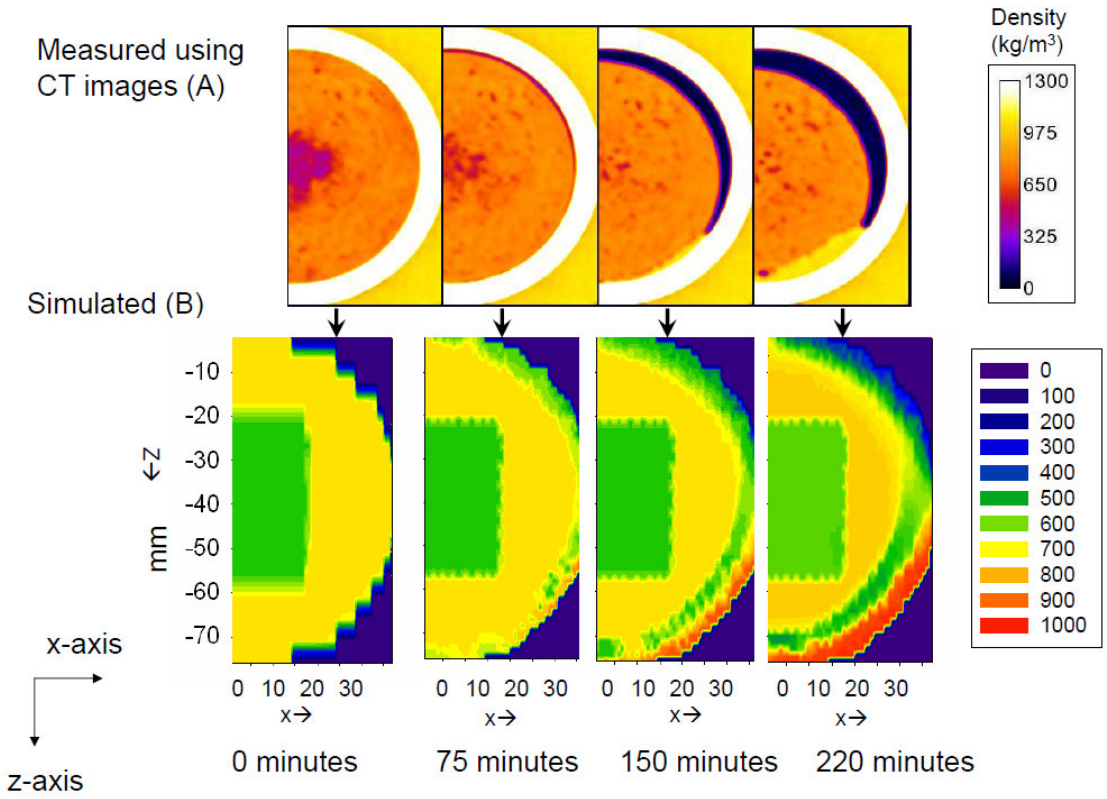

Figure 10. Comparison between measured (A) and predicted (B) density profile of the porous methane hydrate sample with time during depressurization-induced dissociation.

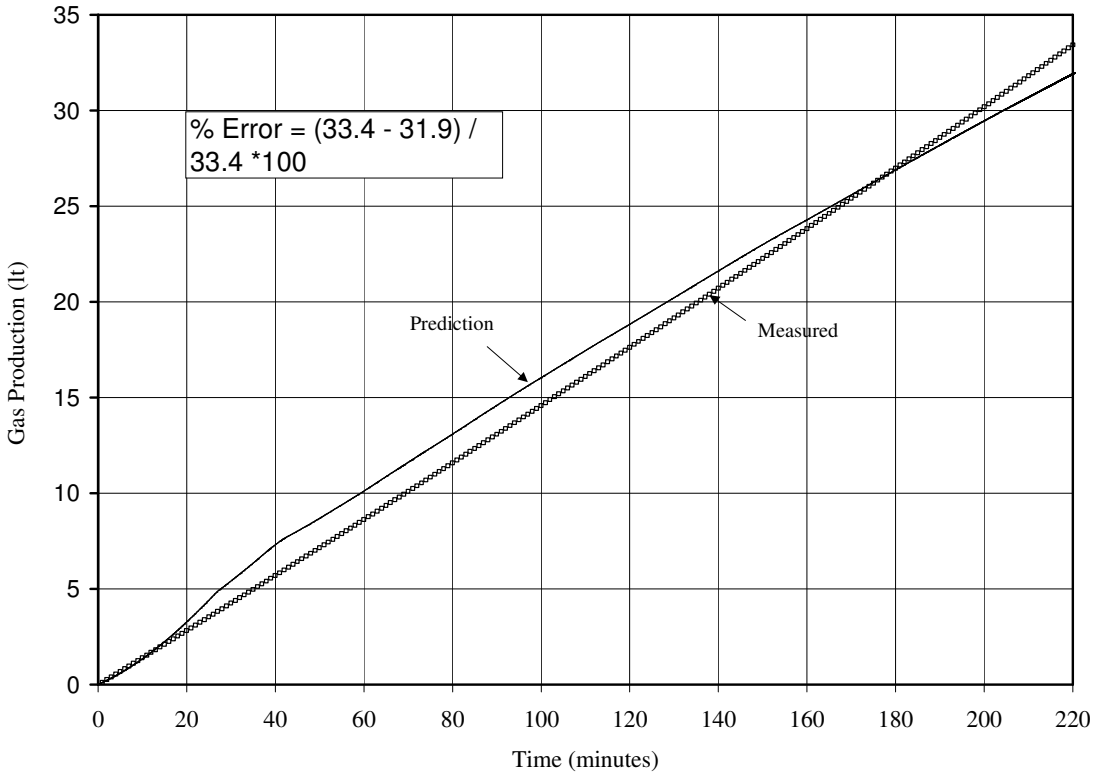

Figure 11. Comparison of predicted and measured methane gas production data with time during depressurization-induced dissociation.

	r * (mm)	S_H	S_A	S_G
Zone1	0-18	0.25	0.14	0.61
Zone2	18-38	0.77	0.02	0.21

* Distance from the center

Table 1. Initial average phase saturations in the heterogeneous porous methane hydrate sample.